nature physics

Article

https://doi.org/10.1038/s41567-023-02080-w

A quantum electromechanical interface for long-lived phonons

In the format provided by the authors and unedited

Supplementary Information: A quantum electromechanical interface for long-lived phonons

Alkim Bozkurt,[1,2] Han Zhao,[1,2] Chaitali Joshi,[1,2] Henry G. Leduc,[3] Peter K. Day,[3] and Mohammad Mirhosseini[1,2]

[1] *The Gordon and Betty Moore Laboratory of Engineering, California Institute of Technology, Pasadena, California 91125*
[2] *Institute for Quantum Information and Matter, California Institute of Technology, Pasadena, California 91125*
[3] *Jet Propulsion Laboratory, California Institute of Technology, Pasadena, California 91109*

(Dated: April 17, 2023)

CONTENTS

I. ELECTROSTATIC INTERACTION

A. Hamiltonian Derivation

The interaction term in the Hamiltonian for a capacitor with mechanically moving electrodes (C_m) is given as

$$H_\mathrm{int} = \frac{\hat{q}^2}{2C_\mathrm{m}}\left(\frac{1}{C_\mathrm{m}}\frac{\partial C_\mathrm{m}}{\partial x}\hat{x}\right). \tag{1}$$

The displacement operator can be written as $\hat{x} = x_\mathrm{zpf}(\hat{b}+\hat{b}^\dagger)$. We have both electrostatic charges due to the external voltage source and RF charge associated with the microwave resonance on top of the capacitor. This leads to a charge operator which can be written as $\hat{q} = iQ_\mathrm{zpf}(\hat{a}-\hat{a}^\dagger)+Q_\mathrm{DC}$. Inserting these operators into the Hamiltonian, we obtain

$$H_\mathrm{int} = \frac{1}{2}\frac{\partial C_\mathrm{m}}{\partial x}x_\mathrm{zpf}\left[i\frac{Q_\mathrm{zpf}}{C_\mathrm{m}}(\hat{a}-\hat{a}^\dagger)+\frac{Q_\mathrm{DC}}{C_\mathrm{m}}\right]^2(\hat{b}+\hat{b}^\dagger). \tag{2}$$

Noting that $Q_{\rm zpf}/C_{\rm m} = V_{\rm zpf}$, $Q_{\rm DC}/C_{\rm m} = V_{\rm DC}$ and expanding the terms

$$H_{\rm int} = \frac{1}{2}\frac{\partial C_{\rm m}}{\partial x} x_{\rm zpf}(\hat{b}+\hat{b}^\dagger)\left[-V_{\rm zpf}^2(\hat{a}-\hat{a}^\dagger)^2 + V_{\rm DC}^2 + 2iV_{\rm zpf}V_{\rm DC}(\hat{a}-\hat{a}^\dagger)\right]. \tag{3}$$

Keeping only the interaction terms between the DC voltage and the RF fields and carrying out the rotating wave approximation for our case of mechanics in resonance with microwave gives us

$$H_{\rm int} = i\frac{\partial C_{\rm m}}{\partial x} x_{\rm zpf}V_{\rm zpf}V_{\rm DC}(\hat{a}\hat{b}^\dagger - \hat{a}^\dagger\hat{b}) = i\hbar g_{\rm em}(\hat{a}\hat{b}^\dagger - \hat{a}^\dagger\hat{b}). \tag{4}$$

This Hamiltonian has the form of an artificial piezoelectric response with an interaction strength

$$\hbar g_{\rm em} = \frac{\partial C_{\rm m}}{\partial x} x_{\rm zpf}V_{\rm zpf}V_{\rm DC}. \tag{5}$$

This constitutes a parametric interaction where the interaction strength scales linearly with the applied external voltage.

Upon obtaining the interaction term, we can write the full Hamiltonian of our system as

$$H/\hbar = \omega_r\hat{a}^\dagger\hat{a} + \omega_m\hat{b}^\dagger\hat{b} + ig_{\rm em}(\hat{a}\hat{b}^\dagger - \hat{a}^\dagger\hat{b}). \tag{6}$$

B. Coherent Response

In probing our cavity-mechanics system, we use a microwave tone. We can write the Langevin equations for eq. (6) as

$$\dot{\hat{a}} = -(i\omega_r + \kappa/2)\,\hat{a} - g_{\rm em}\hat{b} - \sqrt{\kappa_e}\hat{a}_{\rm in} \tag{7}$$

$$\dot{\hat{b}} = -(i\omega_m + \gamma/2)\,\hat{b} + g_{\rm em}\hat{a}. \tag{8}$$

where we have neglected the thermal fluctuations entering the microwave and mechanics, as we are focused on the coherent response of our system.

Taking the Fourier transform of the Langevin equations, we obtain

$$(i\Delta + \kappa/2)\,\hat{a}(\omega) = -g_{\rm em}\hat{b}(\omega) - \sqrt{\kappa_e}\,\hat{a}_{\rm in}(\omega) \tag{9}$$

$$(i\delta + \gamma/2)\,\hat{b}(\omega) = g_{\rm em}\hat{a}(\omega), \tag{10}$$

where $\Delta = \omega_r - \omega$ and $\delta = \omega_m - \omega$. Substituting eq. (10) into eq. (9), we can express the microwave cavity operator as

$$\hat{a}(\omega) = -\frac{\sqrt{\kappa_e}\,\hat{a}_{\rm in}(\omega)}{i\Delta + \kappa/2 + \frac{g_{\rm em}^2}{i\delta+\gamma/2}}. \tag{11}$$

Using input-output theory, we can define the output operator as $\hat{a}_{\rm out}(\omega) = \hat{a}_{\rm in}(\omega) + \sqrt{\kappa_e}\hat{a}(\omega)$. Using eq. (11), we obtain an expression similar to the familiar electromechanically induced transparency (EIT) expression

$$\frac{\hat{a}_{\rm out}(\omega)}{\hat{a}_{\rm in}(\omega)} = 1 - \frac{\kappa_e}{i\Delta + \kappa/2 + \frac{g_{\rm em}^2}{i\delta+\gamma/2}}. \tag{12}$$

We utilize this expression to fit the reflection traces we obtain of the cavity-mechanics system.

C. Coupling Perturbation Theory

Within the framework of cavity electromechanics, we can consider our interaction to be caused by radiation pressure. More precisely, the stored electrical energy in our system changes with the mechanical displacement via the modulation of the capacitance. Looking at the term in the Hamiltonian that leads to electrostatic interaction in eq. (3), we can see that the change in the cross-electrical energy is the origin of this interaction and thus can be used to capture the change in the capacitance. It is possible to express this change in the energy via a perturbative integral, similar to the moving boundary integrals for electromechanical systems [1]. In this perturbative approach, we assume that the displacement of the material boundaries does not change the electric field, but alters the local permittivity leading to an electromechanical coupling rate

$$\hbar g_{em} = x_{\mathrm{zpf}} \oint dA \,\left(\mathbf{Q}(\mathbf{r}) \cdot \hat{n})(\Delta\epsilon \mathbf{E}^{\parallel}(\mathbf{r})_{\mathrm{DC}} \mathbf{E}^{\parallel}(\mathbf{r})_{\mathrm{RF}} \;-\Delta\epsilon^{-1} \mathbf{D}^{\perp}(\mathbf{r})_{\mathrm{DC}} \mathbf{D}^{\perp}(\mathbf{r})_{\mathrm{RF}}\right). \tag{13}$$

Here, $x_{\mathrm{zpf}} = \sqrt{\hbar/2m_{\mathrm{eff}}\omega_m}$ is the zero point fluctuations of displacement and m_{eff} is the effective mass of the acoustic resonator. $\mathbf{Q}(\mathbf{r})$ is the normalized displacement where $\max[\mathbf{Q}(\mathbf{r})] = 1$. $\Delta\epsilon = \epsilon_1 - \epsilon_2$ and $\Delta\epsilon^{-1} = 1/\epsilon_1 - 1/\epsilon_2$ are the electrical permittivity contrast between the two materials that are on the boundary covered by the surface integral. $\mathbf{E}^{\parallel}(\mathbf{r})_{\mathrm{DC}}$ ($\mathbf{E}^{\parallel}(\mathbf{r})_{\mathrm{RF}}$) is the parallel electric field component obtained from electrostatic simulations of the capacitor with V_{DC} (V_{zpf}) applied to the capacitors. Likewise, $\mathbf{D}^{\perp}(\mathbf{r})_{\mathrm{DC}}$ ($\mathbf{D}^{\perp}(\mathbf{r})_{\mathrm{RF}}$) is the perpendicular displacement field obtained from the same simulation. In this expression, the voltage dependence of the coupling is directly embedded in the capacitor voltages used in the simulations. One can alternatively solve for a given voltage (such as 1 V) and then scale the fields appropriately based on V_{DC} and V_{zpf}. For instance, g_0 can be simply obtained by setting $V_{\mathrm{DC}} = 1$ V.

It has been previously observed that the electrical response of the capacitor at DC and RF frequencies may differ from one another [2]. Generally, the charge carriers freeze off at cryogenic temperatures, giving rise to massive resistivity values for silicon [3]. However, in capacitor structures under DC voltages, band bending leads to the formation of a narrow space charge region which effectively screens out the field at the bulk of the silicon [4]. This leads to a DC response which can approximately be modeled by treating silicon as a perfect conductor. On the other hand, our microwave field which oscillates at a frequency above the RC cutoff cannot be screened and silicon behaves like a perfect insulator for these fields.

Taking this into account, only fields perpendicular to the boundaries will exist for the DC field and the integral for the electromechanical coupling can be simplified to.

$$\hbar g_{em} \approx x_{\mathrm{zpf}} \oint dA \,\left(\mathbf{Q}(\mathbf{r}) \cdot \hat{n})(\epsilon_0^{-1} \mathbf{D}^{\perp}(\mathbf{r})_{\mathrm{DC}} \mathbf{D}^{\perp}(\mathbf{r})_{\mathrm{RF}}\right). \tag{14}$$

For our devices with $g_0/2\pi = 45.4$ kHz/V this approach gives us an accurate simulation result of 46 kHz/V. If we were to assume that silicon was an insulator at all frequencies and the field distributions were identical, we would underestimate our coupling strength and obtain 32 kHz/V.

D. Equivalent Circuit Model

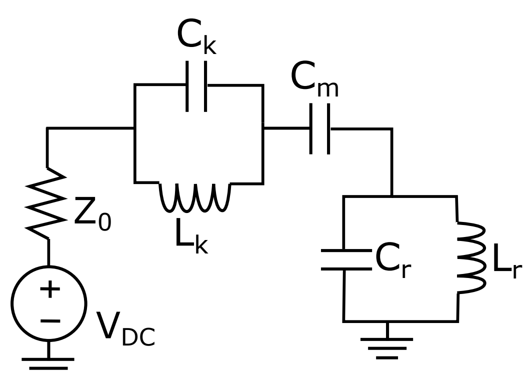

FIG. 1. **Equivalent circuit.** Equivalent electrical circuit of our system.

The calculation of the electromechanical coupling strength via finite element method simulations is sufficient to completely describe the behavior of our system which consists of two coupled resonators. However, obtaining an electrical equivalent circuit for the mechanical resonator is crucial for making the analysis of complex electromechanical circuits more tractable. For this purpose, we model our mechanical resonator by a parallel LC resonator (C_{k},L_{k}) in series with a capacitor C_{m}. This model can be seen in fig. 1, where the coupling to the lumped element microwave resonator (C_{r},L_{r}) is capacitive via C_{m}.

The equivalent mechanical capacitance can be expressed as

$$C_{\mathrm{k}} = \frac{\hbar C_{\mathrm{m}}^2 \omega_m}{2\,\left(\partial_x C_{\mathrm{m}}\, x_{\mathrm{zpf}}\, V_{\mathrm{DC}}\right)^2} - C_{\mathrm{m}}. \tag{15}$$

The equivalent mechanical inductance can be obtained following the calculation of C_{k} by noting that $\omega_m = [L_{\mathrm{k}}(C_{\mathrm{k}} + C_{\mathrm{m}})]^{-1/2}$. This circuit model gives us the correct expression for the electromechanical coupling strength, which is attained by capacitive coupling between the two circuit modes where

$$g_{\mathrm{em}} = \frac{C_{\mathrm{m}}}{2\sqrt{(C_{\mathrm{k}} + C_{\mathrm{m}})(C_{\mathrm{r}} + C_{\mathrm{m}})}} \sqrt{\omega_r \omega_m}. \tag{16}$$

In this capacitive coupling picture, the value of C_{r} primarily sets the zero point fluctuations of voltage for the microwave resonator since we have a small electromechanical participation ratio ($\eta = C_{\mathrm{m}}/(C_{\mathrm{m}} + C_{\mathrm{r}}) \ll 1$). The small participation ratio of our capacitor is caused by the small physical dimensions of our electromechanical capacitor which is commensurate with 1μm transverse acoustic wavelength at 5 GHz. This leads to the electrical energy on top of the electromechanical capacitor being substantially diluted compared to the total electrical energy stored on the microwave resonator.

We express the circuit parameters for device B in Table I. We note that the equivalent circuit model parameters for the mechanical resonator are dependent on the external voltage bias V_{DC}. This scaling is noted in the table, where L_{k} and C_{k} are provided for 1 V.

TABLE I. Equivalent circuit parameters for device B. The mechanical parameters C_{k} and L_{k} are dependent on the applied external voltage. The given values are for 1 V and the dependence on V_{DC} is specified.

Parameter	Value
C_{m}	0.2 fF
C_{r}	12.1 fF
L_{r}	75.8 nH
η	1.5 %
L_{k}	43.5 fH $(1\mathrm{V}/V_{\mathrm{DC}})^2$
C_{k}	21.1 nF $(V_{\mathrm{DC}}/1\mathrm{V})^2$
$f_{r,m}$	5.26 GHz
$g_0/2\pi$	45.4 kHz/V

In the circuit model, one can see that the mechanical resonator is capacitively coupled to the CPW which has an impedance $Z_0 = 50\ \Omega$. This leads to some direct external decay to the CPW. However, even at the maximum voltage we can apply of 25 V, due to our massive equivalent capacitance this readout is at the level of 5 Hz, which is negligible and further emphasizes the need for a microwave cavity to enhance electromechanical readout of mechanics.

II. MICROWAVE DEVICES

A. Microwave Resonator

The $\lambda/4$ tunable microwave resonators in our work are formed by ICP-RIE etching of TiN films ($t \sim 15$ nm) with a sheet kinetic inductance of 40 pH/$\square$ [5], which are sputtered on high resistivity (> 3 kΩ.cm) SOI substrates (device layer thickness 220 nm, manufactured by SEH). The high kinetic inductance TiN films are chosen for two main reasons: (i) obtaining a large impedance ($Z = \sqrt{L/C}$) resonator in order to enhance the electromechanical interaction ($g_{\mathrm{em}} \propto \sqrt{Z}$) and (ii) attaining a high degree of tunability via an external magnetic field to bring the microwave into resonance with mechanics. These goals are satisfied by forming a $\lambda/4$ resonator, with the inductive component realized by a nanowire. The total kinetic inductance in this structure is a function of film properties and geometry

$$L_{\mathrm{k}} = L_{\square} \frac{8}{\pi^2} \frac{l}{w}, \tag{17}$$

where $L_{\square}$ is the sheet inductance, l is the nanowire length and w is the nanowire width. In order to maximize the impedance, we etch our nanowires to be as narrow as possible, which in our case corresponds to a width of

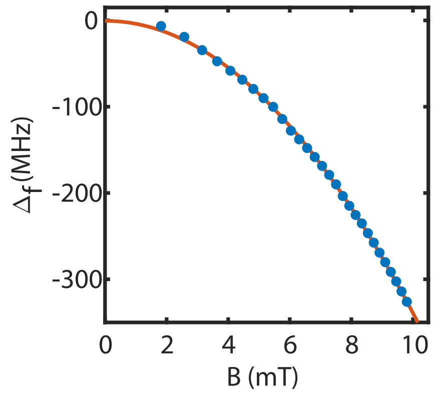

FIG. 2. **Microwave tuning.** Change in the microwave resonance frequency based on the applied external perpendicular magnetic field. The solid line is a parabolic theory fit.

approximately 110 nm. Attempts to reduce wire width below this number led to reduced repeatability in fabrication and a large disorder in resonator frequency.

A current passing through a TiN nanowire modifies the kinetic inductance in a nonlinear fashion

$$L_{\mathrm{k}}(I) = L_{\mathrm{k}}(0)\left[1 + \left(\frac{I}{I_*}\right)^2\right]. \tag{18}$$

where I_* is the critical current of the nanowire. Patterning of the nanowires to form closed loops and application of an external perpendicular magnetic field, provides a 'wireless' means of modifying the kinetic inductance via the screening current induced through the loops [6]. This is the mechanism we us to tune the resonator's frequency.

With these principles in mind, we utilize a ladder-like topology for our microwave resonator. Finite-element method (FEM) simulations indicate that our kinetic inductance excellently matches eq. (17) and we have negligible geometric inductance, leading to a kinetic inductance participation ratio of approximately unity ($>$ 98%). Furthermore, we calculate the impedance of our resonator to be 2.5 kΩ. The calculated lumped element equivalent circuit parameters for the microwave resonator of device B can be seen in Table I. Despite having a substantial impedance, due to our mechanical capacitance being very small, we have a low electrical energy participation ratio for the mechanical capacitor ($\eta = C_{\mathrm{m}}/(C_{\mathrm{m}}+C_{\mathrm{r}})$) of 1.5%. This small participation ratio permits us to connect multiple electromechanical capacitors to our microwave resonator.

Following fabrication, we find the resonance frequencies in good agreement with the device modeling, with a random offset with an approximate mean value of 300 MHz, which we attribute to fabrication disorder in the narrow nanowires. We test the tunability of our devices by applying external magnetic fields via currents passing through a superconducting coil mounted on top of the sample box. For small fractional shifts (normalized to the original frequency), we expect the frequency shift to be given by

$$\Delta_f = -kB^2, \tag{19}$$

where k is a device dependent proportionality constant and B is the external perpendicular magnetic field amplitude [6]. This parabolic dependence is verified for device B on fig. 2. We can tune our device by about 6% of their resonance frequency without causing any substantial degradation of the microwave intrinsic quality factor beyond $\kappa_i/2\pi \sim 500$ kHz.

B. Purcell Filter

In our design, we prioritize redundancy in terms of the number of mechanical resonators by attaching four electromechanical capacitors to a single microwave resonator. This is done to mitigate the impact of frequency shifts caused by fabrication disorder of the microwave resonators, where the different mechanical resonators span roughly 500 MHz (the disorder in the mechanical frequencies is much smaller than the microwave disorder). However, this approach leads to an increased capacitance between our microwave resonator and the CPW, which gives rise to undesirably large external microwave decay. In order to increase the cooperativity of our system and reach the strong-coupling regime, this decay channel has to be suppressed.

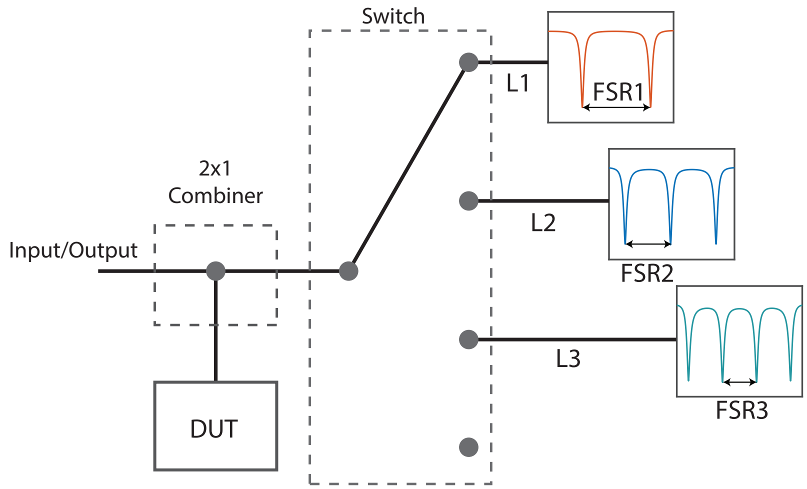

FIG. 3. **Purcell filter.** Circuit diagram of the Purcell filter configuration. The input/output line is attached to a circulator (not shown in the figure) used for investigation of the devices in reflection mode. The final port of the switch is not connected to a transmission line. The transmission lines have different lengths (L1,L2,L3). Their response is depicted as Lorentzian resonances separated by a given FSR that differs for each cable. DUT: Device under test.

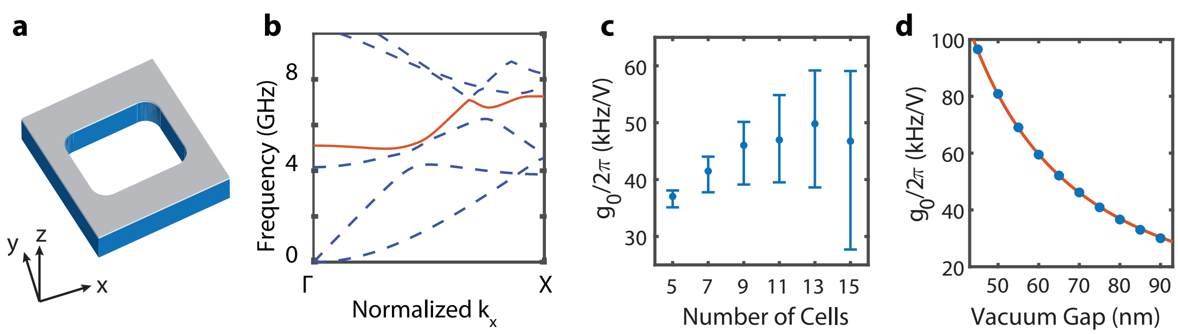

FIG. 4. **Moving capacitor design.** (a) Unit cell of the inner electrode of the electrostatic transducer. The beam is oriented along the x-direction. (b) Unit cell acoustic band diagram. (c) Disorder simulations of coupling strength vs number of unit cells of the inner electrode for $\sigma = 2$ nm disorder and 55 realizations for each data point. The simulations are for a 70-nm vacuum gap. The data is presented as the mean with 2 standard deviation errobars. (d) Average coupling strength vs vacuum gap size for 9 unit cells. The simulated average values are in the presence of fabrication disorder. The fit is $\propto$ gap$^{-1.66}$.

We utilize an off-chip Purcell filter for this purpose as depicted schematically in fig. 3. We place the filter in parallel to our device, where the notch filter reduces the external coupling strength of the microwave resonator. For this purpose, we make use of home-built microwave filters, realized as open transmission lines with a multi-pole spectrum. To get approximate frequency matching between our devices and the filter, we use a mechanical switch that enables us to choose among multiple filters with different free spectral ranges (FSR) between 200-500 MHz. In cases where we get perfect frequency matching between a device and a filter resonance, we can reduce the external decay rate $\kappa_e/2\pi$ to sub-200 kHz levels. Furthermore, we have a port in our switch which is not connected to a transmission line, permitting us to effectively turn our filter off.

III. MECHANICS DESIGN

The mechanical behavior of our structures is investigated via FEM simulations on COMSOL. The inner electrode of the electrostatic transducer is patterned to form a phononic crystal cavity consisting of multiple identical unit cells, with the unit cell depicted in fig. 4a. These unit cells are completely metallized with a 15-nm layer of TiN on top of a

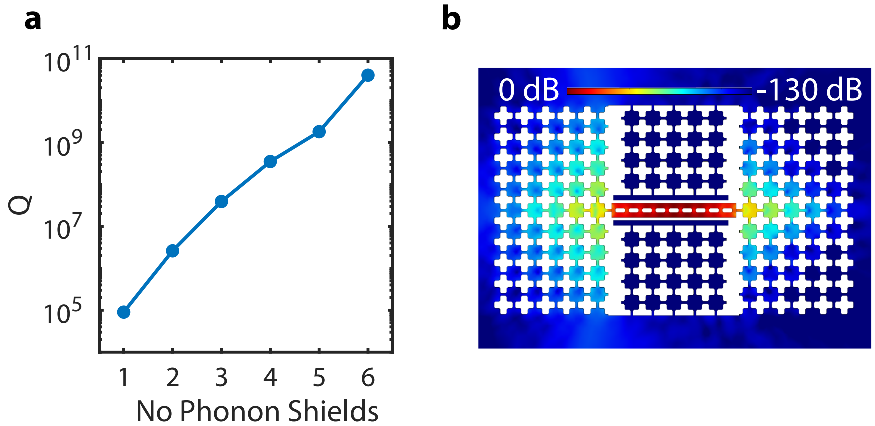

FIG. 5. **Mechanical quality factor.** (a) Radiation limited acoustic quality factor vs the number of phonon shield periods in the absence of disorder. (b) Logarithmic plot of mechanical energy density for 5 shield periods.

220-nm Si membrane (the anisotropic elasticity tensor is used for silicon in simulations following [7]). We are primarily interested in the Γ point of the breathing mode shown by the red band on the unit cell band diagram on fig. 4b. The breathing mode is chosen because it has a displacement profile that significantly modulates the electromechanical capacitance. The Γ mode is further necessary to ensure phase matching of the electromechanical interaction. Once multiple unit cells are attached to form a 1-D chain and are clamped by phononic shields that have a full bandgap, they hybridize to form a supermode that spans all the unit cells, which is our mechanical mode of interest.

Ideally, we would like to have as many unit cells as possible in forming our central electrode since the electromechanical interaction strength scales as $\propto \sqrt{N_{\text{cells}}}$. In practice, however, fabrication disorder leads to mode break-up, limiting the number of cells that can be utilized. We investigate this phenomenon via disorder simulations, which constitute a crucial tool in investigating the disorder-limited properties of periodically patterned acoustic and optical structures [8–10]. The disorder can be modeled as random changes in the center positions and the width of the negative patterns, which are etched to form the actual structure. These random changes are represented as realizations of independent Gaussian random variables with zero mean and standard deviation σ. The precise algorithm is as follows: (i) the center of the etched filleted rectangles are varied by σ in each direction (ii) the height and width of the rectangles are varied by 2σ. Since each simulation represents a given disorder realization, to accurately extract the statistics we simulate multiple instances for a given number of unit cells. We investigate the impact of the disorder on the coupling strength as shown in fig. 4c. In this situation, the changes in the mode profile and potential disorder-induced mode breakup are captured in variations in the coupling strength, which is the experimentally relevant parameter to us. We can see that up until 9 unit cells, g_0 grows with the number of cells. However, beyond this number, the growth rate diminishes and the disorder-induced variations increase substantially. At 9 unit cells and a 70-nm gap, we have a coupling strength of 46^{+4}_{-7} kHz/V which is in excellent agreement with our experimental results. The device parameters for the moving capacitor based on this result is tabulated in table II. Finally, we investigate the dependence of the coupling strength on the vacuum gap as shown in fig. 4d. The fit indicates that the coupling strength is a very strong function of the gap and the scaling is more rapid than that of a parallel plate capacitor.

Since acoustic waves cannot propagate in vacuum, the only radiative leakage pathway is through the silicon substrate. We minimize this loss by clamping our acoustic resonator with a phononic shield that has a complete bandgap. We investigate the effectiveness of the phononic shields in suppressing radiation loss via finite-element simulations, where the continuum of modes in the substrate is modeled by a perfectly matched layer. The simulations provide us with the radiation limited mechanical Q in the absence of fabrication disorder. As depicted in fig. 5a the mechanical quality factor scales nearly exponentially with the number of phononic shields. We have used 5 shield periods in our final design, for which we plot the acoustic energy distribution in fig. 5b.

IV. THERMOMETRY

A. Theory

We perform thermometry by measuring the emission from the microwave and mechanical resonators with a spectrum analyzer. Our Hamiltonian is identical to that of a red-detuned optomechanical system with a large sideband resolution

TABLE II. Parameters of the moving capacitor.

Parameter	Value
m_{eff}	76 fg
x_{zpf}	4.7 fm
k_{eff}	7.5×10^7 N/m
$\partial C/\partial x$	5.76×10^{-10} F/m

($\omega_m/\kappa \gg 1$). Hence, in order to extract the thermal occupancy values for the microwave and mechanical thermal baths, we use the expression for the noise power spectral density following previous electromechanics work [11, 12]. The power spectral density at the output of the amplifier chain is

$$S(\omega) = \hbar\omega 10^{\mathcal{G}/10}\left(n_{\text{add}} + \frac{1}{2} + n_{\text{wg}}\left|\left(1 - \frac{\kappa_e\chi_r}{1+g_{\text{em}}^2\chi_m\chi_r}\right)\right|^2 + n_{\text{b,r}}\frac{\kappa_e\kappa_i|\chi_r|^2}{|1+g_{\text{em}}^2\chi_m\chi_r|^2} + n_{\text{b,m}}\frac{\kappa_e\gamma_i g_{\text{em}}^2|\chi_r|^2|\chi_m|^2}{|1+g_{\text{em}}^2\chi_m\chi_r|^2}\right). \tag{20}$$

Here, $\mathcal{G}$ is the amplifier gain in dB, and n_{add} is the noise added by our amplifiers, which is dominated by the HEMT in our case. In this picture, the microwave resonator interacts with an intrinsic bath of occupancy $n_{\text{b,r}}$ with the rate κ_i and the waveguide having occupancy of n_{wg} with the rate κ_e. Similarly, the mechanical resonator is coupled to an intrinsic bath having occupancy of $n_{\text{b,m}}$ with the rate γ_i. The electromechanical interaction with strength g_{em} will further lead to Purcell decay into the microwave for the mechanics, giving rise to electromechanical cooling. The PSD expression also includes the bare electrical and mechanical susceptibilities which are given as

$$\chi_r^{-1}(\omega) = \kappa/2 - i(\omega - \omega_r) \tag{21}$$

$$\chi_m^{-1}(\omega) = \gamma_i/2 - i(\omega - \omega_m), \tag{22}$$

where ω_r (ω_m) is the microwave (mechanics) resonance frequency. In the weak coupling regime, we can express the mechanics and microwave resonator thermal occupancies as

$$n_r = \frac{\kappa_i n_{\text{b,r}} + \kappa_e n_{\text{wg}}}{\kappa_e + \kappa_i}, \tag{23}$$

$$n_m = \frac{n_{\text{b,m}} + Cn_r}{1+C}. \tag{24}$$

Here, $C = \frac{g_{\text{em}}^2\kappa\gamma_i^{-1}}{\Delta^2+(\kappa/2)^2}$ is the effective cooperativity when the mechanical and microwave resonators are detuned by Δ. In the absence of any detuning and at large bias voltages, the cooperativity becomes large, leading to substantial electromechanical cooling, which makes it challenging to unambiguously find the mechanical intrinsic bath occupancy ($n_{\text{b,m}}$). Therefore, we operate in a low-cooperativity regime (large Δ), which permits precise extraction of thermal bath occupancies. Extraction of the mechanical intrinsic bath occupancy is particularly important for quantum memory applications of our mechanical resonators, as there won't be permanent electromechanical cooling in this scenario and the thermal decoherence rate depends on this intrinsic bath occupancy.

To facilitate the analysis, we simplify the emission due to the mechanics' intrinsic bath in eq. (20) as

$$S_m(\delta) \sim 4\tilde{n}_{\text{m}}\frac{\kappa_e}{\kappa}\frac{\Gamma_{\text{em}}}{\gamma}\frac{(\gamma/2)^2}{\delta^2+(\gamma/2)^2}. \tag{25}$$

Here, $\delta = \omega - \tilde{\omega}_m$ is the detuning between the emission frequency and mechanical resonance frequency, with $\tilde{\omega}_m$ being the mechanical frequency shifted by the electrical spring effect. $\gamma = \gamma_i + \Gamma_{\text{em}}$ is the total mechanical linewidth and $\tilde{n}_{\text{m}} = n_{\text{b,m}}\gamma_i/\gamma$ is the thermal occupancy of the mechanical resonator due to fluctuations of the intrinsic mechanical bath.

To accurately utilize the expressions for the noise power spectral density, it is crucial to take into account the distinction between broadening due to frequency jitter and radiative coupling to an intrinsic bath for the mechanical resonator. To this end, we note that the area underneath $S_m(\delta)$ is proportional to the total Purcell enhanced emission from mechanics, which is given as $\Gamma_{\text{em}}\tilde{n}_{\text{m}}$. Hence, we can see that eq. (25) represents the emission for a mechanical resonator that has a total linewidth γ with arbitrary frequency jitter. To take the distinction between jitter and decay into account, once we have extracted $\tilde{n}_{\text{m}}$, we should use only the mechanical intrinsic decay rate Γ_i to calculate the bath thermal occupancy as

$$n_{\text{b,m}} = \tilde{n}_{\text{m}}\frac{\Gamma_{\text{em}} + \Gamma_i}{\Gamma_i}. \tag{26}$$

We note that due to the small non-zero microwave bath occupancy, we have some emissions from the mechanical resonator due to microwave thermal fluctuations entering the mechanics by electromechanical energy exchange. This emission interferes with that of the microwave resonator and leads to noise squashing, as can be seen in the term in eq. (20) proportional to $n_{\rm b,r}$ [13]. This noise squashing is also taken into account in our analysis to calculate our mechanical bath occupancy correctly.

Following this approach, we can investigate the intrinsic microwave ($n_{\rm b,r}$) and mechanical ($n_{\rm b,m}$) bath occupancies as a function of the cryostat temperature. As seen in fig. 6, as the temperature of the cryostat is increased, both bath temperatures follow the cryostat temperature, indicating the validity of our measurement approach.

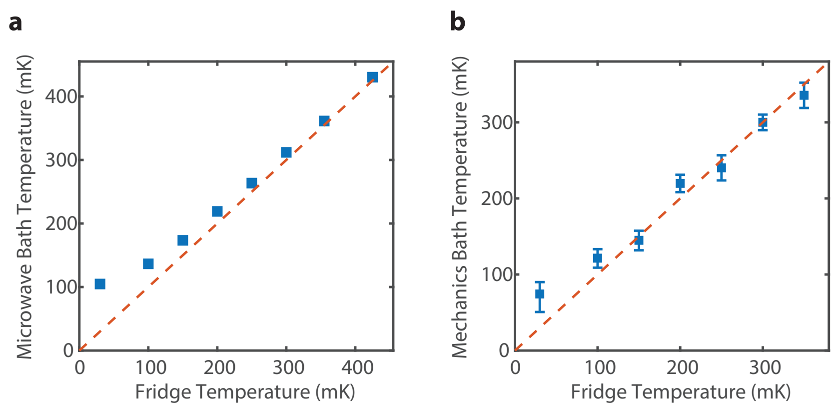

FIG. 6. **Resonator bath thermalization.** The effective temperature for the intrinsic (a) microwave ($n_{\rm b,r}$) and (b) mechanical ($n_{\rm b,m}$) as the cryostat temperature is increased. The dashed line represents perfect thermalization. The presented data is from theory fits with the errorbars indicating $\pm 3\sigma$ confidence interval.

B. Driven Response

We generally do not see significant emission from the mechanical resonator during thermometry, due to the mechanics being deep in its motional ground state. Due to the noise introduced by our HEMT, the spectrum analyzer traces are noisy to an extent that precludes numerically fitting the mechanical emission. Thus, in order to accurately analyze this noisy data and extract the mechanical thermal occupancy, it is crucial to find the mechanical frequency, linewidth, and decay rate at a given voltage.

We achieve this by investigating the driven response of our resonators. Following the application of a coherent tone in resonance with our mechanics, the drive tone is elastically scattered, leading to a delta-like emission from the mechanics and the generation of a coherent phonon population defined as $n_{\rm coh} = |\langle \hat{a} \rangle|^2$. These coherent population dynamics is the origin of the microwave spectrum which can be detected by a VNA. However, the frequency jitter of our system also leads to inelastic scattering of the drive tone. For frequency noise which has a correlation time smaller than the decay rate, we get an emission with the cavity lineshape as the absorbed incoherent phonons lose memory of the drive frequency due to frequency jitter [14]. This inelastic scattering is due to the generation of a number of incoherent phonons in the cavity, whose population is $n_{\rm inc} = \langle \hat{a}^\dagger \hat{a} \rangle - |\langle \hat{a} \rangle|^2$. The incoherent emission enables us to extract the cavity linewidth and frequency via fitting the Lorentzian response. This routine for parameter extraction is repeated prior to mechanics thermometry for each voltage to facilitate accurate calculations with eq. (25) and center the spectrum analyzer detection window.

Apart from extracting the lineshape of the mechanics, we can also use the driven response to measure the intrinsic decay rate Γ_i. The total coherent and incoherent phonon populations are related to the total decay rate $\Gamma_{\rm d} = \Gamma_i + \Gamma_{\rm em}$ and the total linewidth γ as follows [15]

$$\frac{n_{\rm inc}}{n_{\rm coh}} = \frac{\gamma}{\Gamma_{\rm d}} - 1. \tag{27}$$

These phonon populations can be further related to the areas detected via the spectrum analyzer, where S_δ is the area underneath the coherent emission, $S_{\rm bb}$ ($S_{\rm nb}$) is the area underneath the incoherent emission due to broadband (narrow-band) frequency noise. Therefore, the relation between the decay rates can be expressed as

$$\frac{\gamma}{\Gamma_{\rm d}} = 1 + \frac{S_{\rm bb}}{S_\delta}\left(1 - \frac{S_{\rm nb}}{S_\delta}\right), \tag{28}$$

where the broadband frequency noise can be arbitrarily strong, and the narrow-band noise is weak [14]. Subtracting the electromechanical readout rate from the total decay rate, we can calculate Γ_i. The Γ_i obtained in this manner is used to extract the mechanical bath occupancy via eq. (26).

C. Line Calibration

We calibrate the total gain of the output line using thermometry of a 50 Ω cryogenic terminator that is thermalized to the mixing (MXC) stage of the cryostat. The output line consists of a HEMT amplifier (LNF-LNC48C) thermalized to the 4 K stages and a room-temperature amplifier. The MXC stage temperature is raised by reducing cooling power by turning off the turbo to reduce ^{3}He/^{4}He mixture flow and applying heat using the MXC stage heater. With no external input power, we measure the output power from the amplifier chain with a spectrum analyzer at different mixing stage temperatures T_{MXC}. The measured output power has contributions from the thermal noise of the resistor thermalized to the MXC stage, and the HEMT noise is characterized by a fixed noise temperature T_{HEMT}. The total power measured in an IF bandwidth $\Delta\nu_{\mathrm{IF}}$ on the spectrum analyzer is equal to the sum of the Johnson-Nyquist noise from the two sources and is given by,

$$P_{\mathrm{OUT}} = \Delta\nu_{\mathrm{IF}} k_{\mathrm{B}} G_{\mathrm{A}} \left(T_{\mathrm{MXC}} + T_{\mathrm{HEMT}}\right) \tag{29}$$

Here, G_A is the absolute (net) gain factor of the output line, and is a combination of the total gain due to the amplifier chain and losses due to coaxial cables. At $T_{\mathrm{MXC}} = 10$ mK, the measured output power is dominated by HEMT noise. The output gain G_A can be calculated by subtracting the contribution of the HEMT noise from the total output power measured at various T_{MXC}. We perform this measurement at multiple different MXC temperatures between 730 mK and 1.05 K. These measurements' mean and standard deviation are used to obtain G_A. We use a factor $\eta = (\hbar\omega/k_B T)/\left(\exp\left(\hbar\omega/k_B T\right) - 1\right)$ to account for corrections to eq. (29) due to the Bose-Einstein distribution in the regime $\hbar\omega \sim k_B T$ [16]. Using this calibration method, we obtain a net gain of 65.6 ± 0.4 dB for the output line.

D. Pull-in Instability

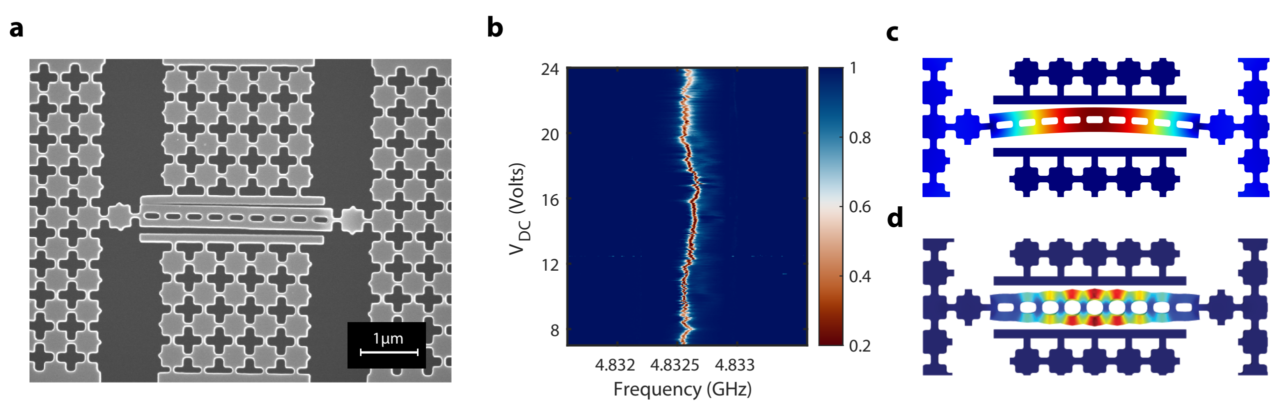

FIG. 7. **Pull-in instability.** (a) Post-measurement SEM image of a transducer device that had permanently broken down. The pull-in phenomenon can be observed at the top-left corner of the electromechanical capacitor, where the vacuum gap has become shut. (b) Mechanical power spectrum with the cavity populated to 10^5 phonons with a strong drive (10^5). The pull-in voltage for the measured device is measured to be around 30 V. (c) Displacement profile of the 120 MHz first order beam mode. (d) Displacement profile of the 5 GHz breathing mode that takes part in the electromechanical interaction.

Post-measurement imaging of the devices which were subject to breakdown indicates that the breakdown behavior is caused by the pull-in of the inner electrode to an outer electrode, as seen in fig. 7. Once the capacitor gap becomes shut, a short resistive leakage path appears, leading to substantial current flow as observed in our leakage current measurements. This 'pull-in' phenomenon is commonly observed in electrostatic actuators. As the bias voltage is increased, the strong electrostatic forces can no longer be offset by the mechanical spring force following a certain gap shrinkage, leading to unstable mechanical dynamics [17]. Furthermore, stiction can render this phenomenon irreversible as we have observed, where removal of the external voltage does not lead to recovery of the device.

In the canonical model of an electrostatic transducer, increasing the bias voltage is accompanied by a continuous shrinkage of the gap, and, consequently, a frequency reduction due to the change in the spring constant [18]. We have measured the frequency of the mechanical mode as a function of the bias voltage (see fig. 7) and fit the frequency dependence on voltage to a quadratic function, obtaining a shift coefficient of 0.5 ± 4.7 Hz/V^2, indicating the absence of significant voltage-dependent frequency shift. This absence of significant frequency shifts can be potentially attributed to the multimode nature of our device. In a canonical parallel plate transducer model, the device supports a single mechanical resonance, which experiences a frequency shift as a result of the electrostatic force from the bias. However, in our device, the displacement caused by the electrostatic force most likely follows the mode profile of the fundamental bending mode (see fig. 7c) of the nanobeam whose frequency is approximately at 120 MHz ($k_{\mathrm{eff}} \sim 2 \times 10^5$ N/m). In comparison, the 5 GHz breathing mode utilized in our experiment (see fig. 7d) is much stiffer ($k_{\mathrm{eff}} \sim 8 \times 10^7$ N/m). Therefore, the change in the breathing mode frequency needs to be modeled by considering a displacement profile dictated by another mode at a vastly different frequency. Such modeling will be a topic of future investigations.

V. MECHANICAL COHERENCE

A. Ringdown Measurements

In performing the ringdown measurements, we use a constant DC drive at a selected voltage level and control the electromechanical readout rate via setting the detuning between the microwave resonator and the mechanics. We populate the mechanical cavity via sending microwave pulses resonant with the mechanical mode. The pulses are synthesized with an arbitrary waveform generator (AWG), and their length is chosen to be sufficiently long to ensure the mechanical population can reach the steady state. Following the drive pulse, we detect the emitted power in a given interval by processing the downconverted signal from a digitizer. A power measurement (as opposed to field-quadrature) is obtained by summing the square of the demodulated I and Q quadrature values in a detection window in an FPGA. This detection window length is set to be much shorter than the reciprocal of mechanical linewidth to ensure we detect all the phonons emitted from the resonator. The multiple consecutive detection windows during a single measurement gives us a ringdown curve. We then proceed to average many instances of the experiment to improve our signal-to-noise (SNR) ratio and obtain our final data. The AWG, digitizer, and FPGA functionalities are realized using a Quantum Machines OPX+ module. We calibrate the digitizer output using the calibrated gain of our output lines and refer the detected voltage levels to the number of phonons in the cavity.

We carry out multiple ringdowns while sweeping the voltage to find the optimal lifetime in a voltage range. These ringdowns are performed at a large number of phonons in order to improve the SNR and make the measurements more tractable. Apart from showing signatures of spectral collisions with TLS that are manifested as deteriorating lifetimes, these measurements enable us to extract statistics about our lifetimes. We can see that for the two devices we have measured, we can reliably obtain lifetimes around 30 μs by slightly optimizing our voltage level. Such a typical ringdown is visualized in fig. 8a. We can further see that the points where we have improved coherence properties do not exhibit extreme sensitivity to the applied voltage. For example, for the voltage value where we have obtained our best lifetime on device A, we can obtain similar lifetimes in a 250 mV range as shown in fig. 8b. We can see similar

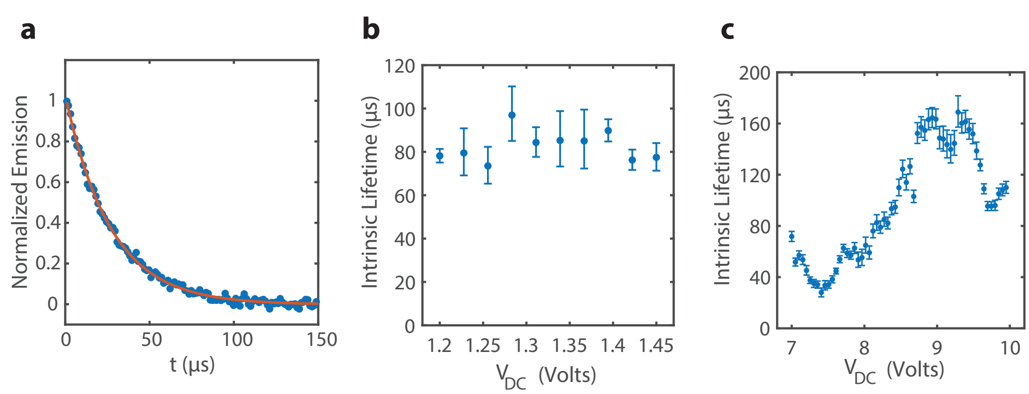

FIG. 8. **Mechanical Lifetime.** (a) Typical ringdown with an intrinsic lifetime of ~ 30 μs. (b) Intrinsic lifetime vs voltage for device A with around 1000 phonons inside the cavity. (c) Intrinsic lifetime vs voltage for device B with around 3000 phonons inside the cavity.

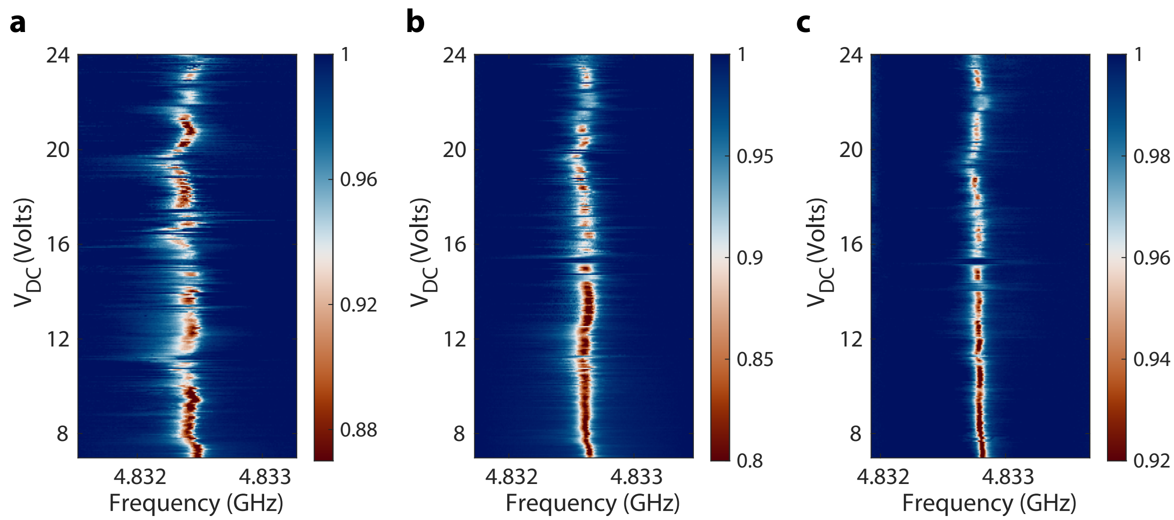

FIG. 9. **Temperature saturation.** Mechanical reflection spectrum at (a) 30mK, (b) 425mK and (c) 850mK. The drive power level is kept constant.

broad regions where the lifetime is enhanced for device B too, as depicted in fig. 8c.

B. Linewidth Characterization

The frequency jitter in our mechanical devices manifests itself as broadening in reflection spectrum measurements. By investigating the dependence of the mechanical linewidth on power level, temperature and external voltage bias, we can better understand the origin of the observed broadening. Similar measurements have been crucial in probing the loss mechanisms of linear microwave [19–22] and mechanical resonators [23–25].

To this end, we investigate the temperature dependence of our mechanical linewidth. As seen in fig. 9, increasing the cryostat temperature leads to narrowing of the mechanical linewidth and the suppression of the frequency shifts. This result indicates that the thermal energy in our cryostat saturates two-level systems (TLS) as the temperature is increased, thereby reducing the mechanical linewidth [26].

In order to strongly saturate TLS, we can populate our mechanical resonator with phonons by using a strong detuned pump. The coupling between the TLS and the mechanical resonator leads to the TLS being driven via the pump and hence saturated [25]. Using a weak probe we can investigate the mechanical linewidth. As seen in fig. 10, the strong drive permits us to substantially saturate the TLS, reaching mechanical linewidths on the order of 10 kHz. The combination of the power and temperature dependence of the linewidth is a strong indicator that TLS induced broadening dominates our total linewidth [26].

Apart from the observation of linewidths at two vastly different power levels indicating the presence of saturation, the power dependence of the linewidth can be investigated for specific voltages. We observe a monotonic saturation behavior of the linewidth as seen in fig. 10c. We can fit this data to a TLS model, with the total linewidth γ be expressed as [20]

$$\gamma = \frac{\gamma_{\mathrm{TLS}}}{\tanh\left(\frac{\hbar\omega}{2k_BT}\right)\sqrt{1+\left(\frac{n}{n_c}\right)^{\beta}}} + \gamma_0, \tag{30}$$

where n is the number of phonons inside the cavity, γ_{TLS} is the TLS limited linewidth, n_c is the critical phonon number, β is a fit parameter and γ_0 is the decay rate from power independent broadening mechanisms. Because the measurements were conducted in the regime $\hbar\omega \gg k_BT$, $\tanh(\frac{\hbar\omega}{2k_BT}) \sim 1$. The fit gives us $\gamma_{\mathrm{TLS}} \sim 240$ kHz and $\gamma_0/2\pi \sim 10$ kHz, indicating that the saturable broadening dominates the total linewidth. The critical phonon number n_c is found to be 2. The parameter β is 0.6, on the order of unity as expected.

In summary our measurements demonstrate: (i) saturation of linewidth with temperature, (ii) saturation of linewidth with power, (iii) observation of random frequency shifts with external voltage bias. We believe that features (i-ii) can be most plausibly explained by saturation of two-level systems [26]. Furthermore, the randomness in the frequency shifts and broadening with voltage are reminiscent of observations of Stark shifts of two-level systems with

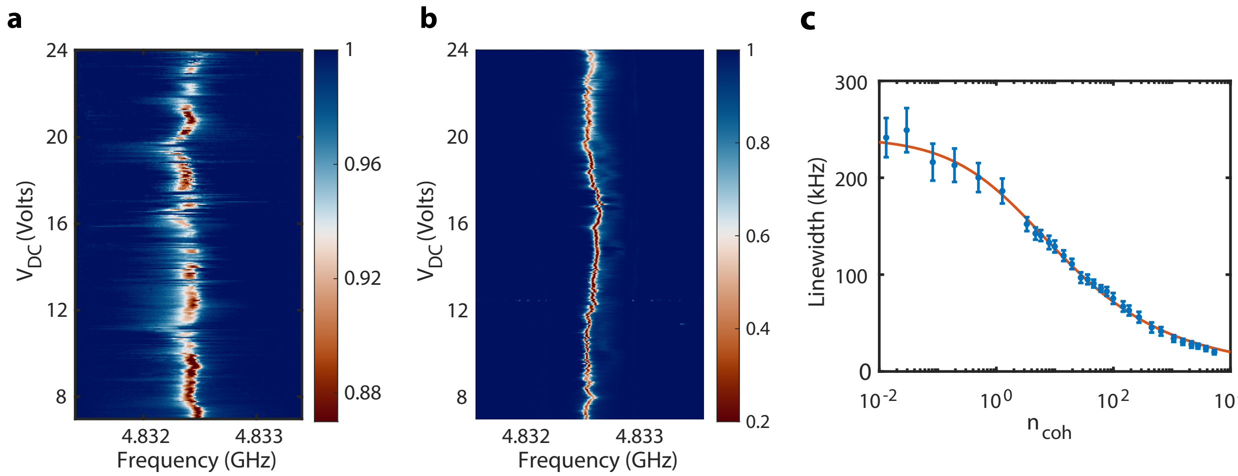

FIG. 10. **Power saturation.** (a) Mechanical reflection spectrum at a probe power corresponding to 100s of phonons. (b) Mechanical reflection spectrum with a strong pump red detuned from the mechanics by ~ 200 kHz. The pump populates the cavity to around 10^5 phonons. The probe power is identical to (a). (c) Dependence of linewidth on the number of coherent phonons for device B at 3 V. The solid line is a fit to the TLS model. Due to ambiguity in the phonon number inside the cavity for VNA measurements, we use the coherent phonon number n_{coh} in our fit (see thermometry section for this distinction). The data is obtained by Lorentzian theory fits, with the 2σ errobars indicating the confidence interval.

external electric fields [27]. Therefore, we believe these features are all consistent with two-level systems being the dominant broadening mechanism.

Beyon TLS, it is important to investigate other broadening mechanisms that may appear due to the large electrostatic fields involved in our experiment. The voltage source in our experiment has a noise magnitude of 200 μV. This noise can potentially lead to fluctuations in the mechanical frequency via the pull-in effect. Using the measured rate of frequency change from thermometry section, we obtain frequency fluctuations on the order of 40 mHz at the highest voltages, which is clearly much smaller than the observed mechanical linewidths. The voltage noise may also introduces fluctuations in the electromechanical readout rate due to the dependence of the coupling strength on the external voltage bias. However, the fractional variation of the fluctuation compared to the mean readout rate is estimated to be around 2×10^{-5}, also too small to play a significant role.

Finally, our experiment's large electrostatic field may lead to the displacement of atoms or trapped charges at the surfaces. However, any possible signatures of such an effect would scale directly with the external voltage (due to the increased electrostatic force). We do not see any global trend where the frequency jitter becomes worse with increased voltage in our data (see fig. 10a). Additionally, we find the voltage-dependent changes in frequency and linewidth repeatable over measurements separated by large time scales (multiple days), which is not consistent with permanent dislocation of atoms or trapped charges [28].

C. TLS Model

The standard tunneling model provides a description of the interaction of TLS with acoustic and electrical fields [26]. We will utilize this model, in conjunction with previous reports of TLS parameters in order to calculate approximate interaction rates between TLS and various fields present in our system. These calculations will serve the purpose of better contextualizing the parameter regime of our TLS interactions compared to other superconducting and mechanical devices.

The TLS is modeled as two potential wells having an asymmetry energy ϵ and a tunneling energy Δ, which leads to a TLS energy of $E = \sqrt{\Delta^2 + \epsilon^2}$. The interaction of TLS with external fields is via modification of its asymmetry energy

$$\epsilon = 2\gamma \cdot \mathbf{S} + 2\mathbf{p} \cdot \mathbf{E} + \epsilon_0, \tag{31}$$

where γ is the mechanical deformation potential around 1 eV in magnitude [29, 30], $\mathbf{S}$ is the external strain field, $\mathbf{p}$ is the TLS dipole moment of roughly 1 Debye [31, 32], $\mathbf{E}$ is the external electric field and ϵ_0 is the residual asymmetry from the environment.

The dependence of the asymmetry energy on the electric field enables us to Stark shift the frequency of TLS via the voltage applied on our electromechanical capacitor. The tuning rate can be calculated as

$$\delta E = 2\frac{\epsilon}{E}\mathbf{p}\cdot\mathbf{E} \tag{32}$$

We use ϵ/E of 0.5 in our analysis following [33]. The narrow vacuum gap capacitors give rise to large electric fields approaching 5×10^{6} V/m, leading to a steep tuning rate of $\delta E/h \approx$ 25 GHz/V.

Apart from Stark shifts, the electric dipole of the TLS also leads to $\mathbf{p}\cdot\mathbf{E}$ coupling to the microwave fields. The zero-point fluctuations of voltage in our microwave resonator is approximately 10 μV, with maximum electric field values of roughly 50 V/m on the interfaces, leading to a TLS-microwave coupling of 250 kHz.

Due to the substantial acoustic susceptibility of TLS, strain coupling constitutes an important mechanism for mechanics-TLS interactions. The coupling strength can be written as

$$\hbar\lambda = \gamma\frac{\Delta}{E}S_{\mathrm{zpf}} \tag{33}$$

where S_{zpf} is the zero-point fluctuations of strain associated with our mechanical mode [33]. This quantity is related to the strain mode volume of our mechanical mode

$$S_{\mathrm{zpf}} = \left(\frac{\hbar\omega_m}{2\mathcal{E}V_m}\right)^{1/2} \tag{34}$$

where $\mathcal{E}$ is the Young's modulus and V_m is the strain mode volume. Due to the small physical dimensions of our mechanical resonator, we have an extremely small strain mode volume of 6×10^{-3} μm^3 and a corresponding S_{zpf} of 4×10^{-8} m/m. This causes a strain coupling strength of $\lambda/2\pi \sim 9$ MHz, which clearly dominates other coupling mechanisms to TLS for the mechanical resonator.

Using our strain mode volume and a TLS density of 10^{45} J^{-1}m^{3} [33], we can obtain a TLS density of approximately 3/GHz, demonstrating our small mode volume giving rise to a small TLS spectral density.

---

[1] A. Pitanti, J. M. Fink, A. H. Safavi-Naeini, J. T. Hill, C. U. Lei, A. Tredicucci, and O. Painter, Strong opto-electro-mechanical coupling in a silicon photonic crystal cavity, Optics Express **23**, 3196 (2015).

[2] R. Van Laer, R. N. Patel, T. P. McKenna, J. D. Witmer, and A. H. Safavi-Naeini, Electrical driving of X-band mechanical waves in a silicon photonic circuit, APL Photonics **3**, 086102 (2018).

[3] E. Gutiérrez-D., J. Deen, and C. Claeys, in *Low Temperature Electronics*, edited by E. A. Gutiérrez-D., M. J. Deen, and C. Claeys (Academic Press, San Diego, 2001).

[4] A. Beckers, F. Jazaeri, and C. Enz, Cryogenic MOSFET Threshold Voltage Model, in *ESSDERC 2019 - 49th European Solid-State Device Research Conference (ESSDERC)* (2019) pp. 94–97.

[5] The unit H/□ (Henry per square) captures the dependence of inductance to the number of squares in a wire. For a wire of length l and width w, the number of squares equals l/w.

[6] M. Xu, X. Han, W. Fu, C.-L. Zou, and H. X. Tang, Frequency-tunable high- Q superconducting resonators via wireless control of nonlinear kinetic inductance, Applied Physics Letters **114**, 192601 (2019).

[7] J. Chan, A. H. Safavi-Naeini, J. T. Hill, S. Meenehan, and O. Painter, Optimized optomechanical crystal cavity with acoustic radiation shield, Applied Physics Letters **101**, 081115 (2012).

[8] N. Le Thomas, Z. Diao, H. Zhang, and R. Houdré, Statistical analysis of subnanometer residual disorder in photonic crystal waveguides: Correlation between slow light properties and structural properties, Journal of Vacuum Science & Technology B **29**, 051601 (2011).

[9] M. Minkov, U. P. Dharanipathy, R. Houdré, and V. Savona, Statistics of the disorder-induced losses of high-Q photonic crystal cavities, Optics Express **21**, 28233 (2013).

[10] G. S. MacCabe, *Phonon Dynamics and Damping in Three-Dimensional Acoustic Bandgap Cavity-Optomechanical Resonators*, Ph.D. thesis, California Institute of Technology (2019).

[11] J. D. Teufel, T. Donner, D. Li, J. W. Harlow, M. S. Allman, K. Cicak, A. J. Sirois, J. D. Whittaker, K. W. Lehnert, and R. W. Simmonds, Sideband cooling of micromechanical motion to the quantum ground state, Nature **475**, 359 (2011).

[12] J. M. Fink, M. Kalaee, A. Pitanti, R. Norte, L. Heinzle, M. Davanço, K. Srinivasan, and O. Painter, Quantum electromechanics on silicon nitride nanomembranes, Nature Communications **7**, 12396 (2016).

[13] A. H. Safavi-Naeini, J. Chan, J. T. Hill, S. Gröblacher, H. Miao, Y. Chen, M. Aspelmeyer, and O. Painter, Laser noise in cavity-optomechanical cooling and thermometry, New Journal of Physics **15**, 035007 (2013).

[14] Y. Zhang, J. Moser, J. Güttinger, A. Bachtold, and M. I. Dykman, Interplay of Driving and Frequency Noise in the Spectra of Vibrational Systems, Physical Review Letters **113**, 255502 (2014).

[15] K. Koshino, Theory of resonance fluorescence from a solid-state cavity QED system: Effects of pure dephasing, Physical Review A **84**, 033824 (2011).
[16] H. Nyquist, Thermal Agitation of Electric Charge in Conductors, Physical Review **32**, 110 (1928).
[17] R. W. Johnstone and M. Parameswaran, *An Introduction to Surface Micromachining* (Springer US, Boston, MA, 2004).
[18] Y. He, J. Marchetti, C. Gallegos, and F. Maseeh, Accurate fully-coupled natural frequency shift of mems actuators due to voltage bias and other external forces, in *Technical Digest. IEEE International MEMS 99 Conference. Twelfth IEEE International Conference on Micro Electro Mechanical Systems (Cat. No. 99CH36291)* (IEEE, 1999) pp. 321–325.
[19] M. Sandberg, M. R. Vissers, J. S. Kline, M. Weides, J. Gao, D. S. Wisbey, and D. P. Pappas, Etch induced microwave losses in titanium nitride superconducting resonators, Applied Physics Letters **100**, 262605 (2012).
[20] J. M. Sage, V. Bolkhovsky, W. D. Oliver, B. Turek, and P. B. Welander, Study of loss in superconducting coplanar waveguide resonators, Journal of Applied Physics **109**, 063915 (2011).
[21] H. Wang, M. Hofheinz, J. Wenner, M. Ansmann, R. Bialczak, M. Lenander, E. Lucero, M. Neeley, A. O'Connell, D. Sank, *et al.*, Improving the coherence time of superconducting coplanar resonators, Applied Physics Letters **95**, 233508 (2009).
[22] M. R. Vissers, J. Gao, D. S. Wisbey, D. A. Hite, C. C. Tsuei, A. D. Corcoles, M. Steffen, and D. P. Pappas, Low loss superconducting titanium nitride coplanar waveguide resonators, Applied Physics Letters **97**, 232509 (2010).
[23] T. Faust, J. Rieger, M. J. Seitner, J. P. Kotthaus, and E. M. Weig, Signatures of two-level defects in the temperature-dependent damping of nanomechanical silicon nitride resonators, Physical Review B **89**, 100102 (2014).
[24] R. Manenti, M. Peterer, A. Nersisyan, E. Magnusson, A. Patterson, and P. Leek, Surface acoustic wave resonators in the quantum regime, Physical Review B **93**, 041411 (2016).
[25] G. Andersson, A. L. O. Bilobran, M. Scigliuzzo, M. M. de Lima, J. H. Cole, and P. Delsing, Acoustic spectral hole-burning in a two-level system ensemble, npj Quantum Information **7**, 1 (2021).
[26] C. Müller, J. H. Cole, and J. Lisenfeld, Towards understanding two-level-systems in amorphous solids: Insights from quantum circuits, Reports on Progress in Physics **82**, 124501 (2019).
[27] J. Lisenfeld, A. Bilmes, A. Megrant, R. Barends, J. Kelly, P. Klimov, G. Weiss, J. M. Martinis, and A. V. Ustinov, Electric field spectroscopy of material defects in transmon qubits, npj Quantum Information **5**, 105 (2019).
[28] P. Mohanty, D. Harrington, K. Ekinci, Y. Yang, M. Murphy, and M. Roukes, Intrinsic dissipation in high-frequency micromechanical resonators, Physical Review B **66**, 085416 (2002).
[29] B. Golding and J. E. Graebner, Phonon echoes in glass, Physical Review Letters **37**, 852 (1976).
[30] G. J. Grabovskij, T. Peichl, J. Lisenfeld, G. Weiss, and A. V. Ustinov, Strain tuning of individual atomic tunneling systems detected by a superconducting qubit, Science **338**, 232 (2012).
[31] B. Sarabi, A. N. Ramanayaka, A. L. Burin, F. C. Wellstood, and K. D. Osborn, Projected dipole moments of individual two-level defects extracted using circuit quantum electrodynamics, Physical review letters **116**, 167002 (2016).
[32] J. D. Brehm, A. Bilmes, G. Weiss, A. V. Ustinov, and J. Lisenfeld, Transmission-line resonators for the study of individual two-level tunneling systems, Applied Physics Letters **111**, 112601 (2017).
[33] T. Ramos, V. Sudhir, K. Stannigel, P. Zoller, and T. J. Kippenberg, Nonlinear Quantum Optomechanics via Individual Intrinsic Two-Level Defects, Physical Review Letters **110**, 193602 (2013).